Ocean Dynamics
DOI 10.1007/s10236-005-0050-1

Hervé Giordani · Louis Prieur · Guy Caniaux

Advanced insights into sources of vertical velocity in the ocean

Received: 4 July 2005 / Accepted: 7 November 2005

Abstract Estimating vertical velocity in the oceanic upper layers is a key issue for understanding ocean dynamics and the transport of biogeochemical elements. This paper aims to identify the physical sources of vertical velocity associated with sub-mesoscale dynamics (fronts, eddies) and mixed-layer depth (MLD) structures, using (a) an ocean adaptation of the generalized **Q**-vector form of the ω-equation deduced from a primitive equation system which takes into account the turbulent buoyancy and momentum fluxes and (b) an application of this diagnostic method for an ocean simulation of the Programme Océan Multidisciplinaire Méso Echelle (POMME) field experiment in the North-Eastern Atlantic. The approach indicates that w-sources can play a significant role in the ocean dynamics and strongly depend on the dynamical structure (anticyclonic eddy, front, MLD, etc.). Our results stress the important contribution of the ageostrophic forcing, even under quasi-geostrophic conditions. The turbulent w-forcing was split into two components associated with the spatial variability of (a) the buoyancy and momentum (Ekman pumping) surface fluxes and (b) the MLD. Process (b) represents the trapping of the buoyancy and momentum surface energy into the MLD structure and is identified as an atmosphere/oceanic mixed-layer coupling. The momentum-trapping process is 10 to 100 times stronger than the Ekman pumping and is at least 1,000 times stronger than the buoyancy w-sources. When this decomposition is applied to a filamentary mixed-layer structure simulated during the POMME experiment, we find that the associated vertical velocity is created by trapping the surface wind-stress energy into this structure and not by Ekman pumping.

Keywords Generalized Ω-equation · **Q**-vector formulation · Turbulent fluxes · Submesoscale structures · Mixed-layer processes/dynamic

Responsible Editor: Bernard Barnier

H. Giordani (✉) · G. Caniaux
Centre National de Recherches,
Météorologiques, Météo-France,
42 Av. G. Coriolis, 31057 Toulouse, Cedex 01, France
e-mail: herve.giordani@meteo.fr

L. Prieur
Laboratoire d'Océanographie de Villefranche,
BP 28, 06234 Villefranche-sur-mer, France

1 Introduction

Knowledge of the mesoscale and sub-mesoscale distribution of vertical velocity in the ocean is of primary importance if one wants to gain insight into the behaviour of the circulation and fine density structures associated with fronts, meanders and interacting eddies (Pollard and Regier 1992; Strass 1994). The dynamics of the vertical circulation at these oceanic structures have important consequences on the transport of properties across the thermocline (Leach 1987; Fischer et al. 1989). Another mesoscale and sub-mesoscale feature of interest is the primary production in the ocean and the horizontal distribution of phytoplankton and chlorophyll. These phenomena are typically driven by near-surface mesoscale and sub-mesoscale upwelling (Lévy et al. 2005). Methods for diagnosing the mesoscale distribution of vertical velocity have been widely discussed in the literature, and an unambiguous conclusion is that the **Q**-vector version of the ω-equation (Hoskins et al. 1978) is the best approach in terms of stability and accuracy (Tintoré et al. 1991; Fiekas et al. 1994; Strass 1994). The **Q**-vector approach was developed from the concept of Thermal Wind Imbalance (**TWI** hereafter) in the Quasi-Geostrophic (QG) system, initially to study atmospheric frontogenesis. The Hoskins **Q**-vector QG form of the vertical velocity is a diagnostic equation that relates at any instant the vertical motion with the production rate of **TWI**. In QG theory, the role of ageostrophic motion is to restore thermal-wind balance that the geostrophic motion is tending to destroy.

Several authors have shown that the standard QG ω-equation has serious limitations for estimating the ageo-

strophic vertical velocity. For instance, when using the Geostrophic Momentum (GM) ω-equation, Pinot et al. (1996) and Keyser and Pecnick (1987) pointed out the necessity of including higher order dynamics than quasi-geostrophy to take into account ageostrophic advection occurring at oceanic and atmospheric fronts. Nevertheless, the QG ω-equation has often been applied to ocean fronts of even a large Rossby number, therefore violating the QG approximation.

The most advanced expressions of the ω-equation were established for the atmospheric primitive equations (PE) system, i.e. for a hydrostatic, inviscid, isentropic, unsatured atmosphere and Boussinesq flow on the *f*-plane (Davies-Jones 1991; Viùdez et al. 1996). These approaches include the ageostrophic sources of vertical velocity, which represent the retroaction of the ageostrophic circulation on itself. These sources, which are neglected in the QG and GM approaches, can play a crucial role for strongly ageostrophic flows with large Rossby numbers (fronts, eddies, filaments). The generalized ω-equations are very powerful because they allow physical insights into the relationship between the actual vertical shear of the horizontal current/wind (which is viewed as the horizontal pseudo-vorticity) and the thermal wind (which is a measure of the horizontal density gradient). However, their formulation does not take into account the turbulent buoyancy and momentum forcing associated with diffusion or convection, which is especially important in oceanic studies. In addition, the equations were not inverted in the full 3D version (in contrast to the QG formulation of Pinot et al. 1996) with all or each of the separate forcing terms.

To understand the dynamics of the oceanic upper layers, in particular the dynamics induced by the atmospheric-mixed-layer coupling, this paper applies the generalized **Q**-vector ω-equation developed by Giordani (1997) and Giordani and Planton (2000) for the atmosphere. This generalized ω-equation is deduced from the 3D PE system and takes into account the turbulent buoyancy and momentum fluxes (Section 2). Advanced studies on the impact of turbulent fluxes on the mixed-layer vertical velocity are conducted in Section 3, using an analytical approach that yields important findings for the ocean–atmosphere coupling. Based on this diagnostic ω-equation, Section 4 carefully analyses the processes that induce vertical velocities in the mesoscale and sub-mesoscale structures simulated in a 3D PE model (Giordani et al. 2005a,b) during the Programme Océan Multidisciplinaire Méso Echelle (POMME) experiment (Mémery et al. 2005). The POMME experiment was devoted to studying the effects of mesoscale structures on water mass subduction in the North-Eastern Atlantic from September 2000 to October 2001.

2 The generalized Q-vector formulation

The factors that differentiate the fluid from the thermal-wind balance in the PE equations system are detailed in Giordani (1997) and Giordani and Planton (2000) and are briefly outlined in this section. The important point here is that the momentum and buoyancy turbulent fluxes are taken into account in the horizontal momentum and density equations, respectively. The momentum, the density and the thermal-wind balance equations are written in the oceanic local reference frame (x, y, z) for hydrostatic and Boussinesq flow on the *f*-plane:

Momentum equations:

$$\begin{cases} \dfrac{du}{dt} = fv_{ag} - \dfrac{1}{\rho}\dfrac{\partial_{\tau_{x\alpha_i}}}{\partial\alpha_i} \; where \; \tau_{x\alpha_i} = \rho\left(\overline{u'^2}; \overline{u'v'}; \overline{u'w'}\right) \\ \dfrac{dv}{dt} = -fu_{ag} - \dfrac{1}{\rho}\dfrac{\partial_{\tau_{y\alpha_i}}}{\partial\alpha_i} \; where \; \tau_{y\alpha_i} = \rho\left(\overline{v'u'}; \overline{v'^2}; \overline{v'w'}\right) \end{cases} \tag{1}$$

$\tau_{x\alpha_i}$ and $\tau_{y\alpha_i}$ are the turbulent momentum fluxes in the ocean and $\mathbf{U}(u, v)$, $\mathbf{U}_g(u_g, v_g)$, $\mathbf{U}_{ag}(u_{ag}, v_{ag}) = \mathbf{U}-\mathbf{U_g}$ are the horizontal, the geostrophic and the ageostrophic currents, respectively, ρ is the density and $\frac{d}{dt}$ is the 3D material derivative.

Density equation:

$$\begin{cases} \dfrac{d\rho}{dt} = -\dfrac{\partial F_{\rho\alpha_i}}{\partial\alpha_i} \\ F_{\rho\alpha_i} = \left(\overline{u'\rho'}; \overline{v'\rho'}; \overline{w'\rho'}\right) \end{cases} \tag{2}$$

$F_{\rho\alpha_i}$ are the turbulent buoyancy fluxes in the ocean.

In PE systems, only the vertical fluxes are taken into account $\left(\overline{w'\rho'}, \overline{w'u'}, \overline{w'v'}\right)$, which are parameterized as $\overline{w'X'} = -K\partial_z\overline{X}$, where K is the vertical mixing coefficient (Gaspar et al. 1990).

For an ocean in geostrophic balance, the vertical derivatives of the current components $\mathbf{U}_g(u_g, v_g)$ are given by the thermal-wind equations

$$\begin{cases} f\dfrac{\partial u_g}{\partial z} = \dfrac{g}{\rho}\dfrac{\partial\rho}{\partial y} \\ f\dfrac{\partial v_g}{\partial z} = -\dfrac{g}{\rho}\dfrac{\partial\rho}{\partial x} \end{cases} \tag{3}$$

The departure from this thermal-wind relation for a non-geostrophic current $\mathbf{U}(u, v)$ is thus expressed as:

$$\begin{cases} TWI(x) = f\dfrac{\partial u}{\partial z} - \dfrac{g}{\rho}\dfrac{\partial\rho}{\partial y} = f\dfrac{\partial u_{ag}}{\partial z} \\ TWI(y) = f\dfrac{\partial v}{\partial z} + \dfrac{g}{\rho}\dfrac{\partial\rho}{\partial x} = f\dfrac{\partial v_{ag}}{\partial z} \end{cases} \tag{4}$$

The vector **TWI** represents the thermal-wind imbalance and its components are part of the ageostrophic horizontal pseudo-vorticity vector (−TWI(y)/f, TWI(x)/f). The differ-

ence between horizontal pseudo-vorticity and vorticity is due to the terms $\partial_y w$ and $-\partial_x w$, respectively. From the material derivative of **TWI**, we infer a diagnostic system for the complete ageostrophic circulation $\mathbf{U}_{ag}(u_{ag}, v_{ag}, w)$ developed in Giordani (1997) and Giordani and Planton (2000). The combination of these equations and the mass conservation ($\partial_x u + \partial_y v + \partial_z w = 0$, incompressible form) generalizes the Hoskins et al. (1978) form of the vertical velocity. The generalized form of the **Q**-vector ω-equation proposed in this paper is expressed as:

$$f^2 \frac{\partial^2 w}{\partial z^2} + \nabla_h \left(N^2 \cdot \nabla_h w \right) = \nabla \cdot \mathbf{Q} \tag{5}$$

where

$$\begin{cases} N^2 = -\frac{g}{\rho}\frac{\partial \rho}{\partial z} \\ \mathbf{Q} = \mathbf{Q}_{th} + \mathbf{Q}_{dm} + \underbrace{2\mathbf{Q}_{tg} + \mathbf{Q}_{tag}}_{\mathbf{Q}_{tw}} + \mathbf{Q}_{dag} + \mathbf{Q}_{dr} \end{cases} \tag{6}$$

The five forcings of the vertical velocity are the divergence of each **Q**-vector, whereas the QG form established by Hoskins et al. (1978) contains only the geostrophic forcing $\nabla.(2\mathbf{Q}_{tg})$. The definition and physical interpretation of each the **Q**-vectors are given below. This generalized form of the ω-equation allows us to quantify many more physical processes producing vertical velocity and is consequently more suitable for studying the ageostrophic circulation in fronts, eddies and in the ocean mixed-layer than the more restrictive QG form. Note that this form preserves the Hoskins formalism, which is an important point for numerically deducing w. In practice, $L = f^2 \frac{\partial^2}{\partial z^2} + N^2 \nabla_h^2$ is an elliptic operator that is inverted to infer the vertical velocity from $w = L^{-1}.\nabla.\mathbf{Q}$. Equation (5) has a unique solution if boundary conditions are known for all the domain. In this way, the solutions depend only on the accuracy of the **Q**-vector forcing.

Forcing terms of the ageostrophic circulation

The **Q**-vectors of Eq. (6) are separated into *turbulent* and *dynamic* forcing as follows:

Turbulent forcings

Buoyancy:

$\mathbf{Q}_{th}$

$$\begin{cases} Q_{thx} = -\frac{g}{\rho}\frac{\partial}{\partial x}\left(\frac{\partial F_{\rho\alpha_i}}{\partial_{\alpha_i}}\right) \\ Q_{thy} = -\frac{g}{\rho}\frac{\partial}{\partial y}\left(\frac{\partial F_{\rho\alpha_i}}{\partial_{\alpha_i}}\right) \end{cases} \tag{7}$$

Momentum:

$\mathbf{Q}_{dm}$

$$\begin{cases} Q_{dmx} = f\frac{\partial}{\partial z}\left(\frac{1}{\rho}\frac{\partial \tau_{y\alpha_i}}{\partial \alpha_i}\right) \\ Q_{dmy} = -f\frac{\partial}{\partial z}\left(\frac{1}{\rho}\frac{\partial \tau_{x\alpha_i}}{\partial \alpha_i}\right) \end{cases} \tag{8}$$

Dynamic forcings

Kinematic deformation:

$\mathbf{Q}_{tw}$

$$\begin{cases} Q_{twx} = \frac{g}{\rho}\left(\frac{\partial u}{\partial x}\frac{\partial \rho}{\partial x} + \frac{\partial v}{\partial x}\frac{\partial \rho}{\partial y}\right) \\ Q_{twy} = \frac{g}{\rho}\left(\frac{\partial v}{\partial y}\frac{\partial \rho}{\partial y} + \frac{\partial u}{\partial y}\frac{\partial \rho}{\partial x}\right) \end{cases} \tag{9}$$

TWI deformation:

$\mathbf{Q}_{dag}$

$$\begin{cases} Q_{dagx} = f\left(\frac{\partial v}{\partial x}\frac{\partial u_{ag}}{\partial z} - \frac{\partial u}{\partial x}\frac{\partial v_{ag}}{\partial z}\right) \\ Q_{dagy} = f\left(\frac{\partial v}{\partial y}\frac{\partial u_{ag}}{\partial z} - \frac{\partial u}{\partial y}\frac{\partial v_{ag}}{\partial z}\right) \end{cases} \tag{10}$$

TWI trend:

$\mathbf{Q}_{dr}$

$$\begin{cases} Q_{drx} = \frac{d}{dt}\left(f\frac{\partial v_{ag}}{\partial z}\right) \\ Q_{dry} = -\frac{d}{dt}\left(f\frac{\partial u_{ag}}{\partial z}\right) \end{cases} \tag{11}$$

Physical interpretation of the **Q**-vectors

The kinematic deformation vector $\mathbf{Q}_{tw}$, also named the frontogenesis vector, represents the temporal change in the horizontal density gradient induced by the total horizontal current field. The forcings $\mathbf{Q}_{tg}$ and $\mathbf{Q}_{tag}$ are the geostrophic and ageostrophic components of $\mathbf{Q}_{tw}$, which are the products of the geostrophic and ageostrophic velocity gradient tensor with the density gradient, respectively. In QG theory, **TWI** is cancelled instantaneously by the ageostrophic circulation, so that only the $\mathbf{Q}_{tg}$ forcing is considered.

The **TWI** deformation forcing $\mathbf{Q}_{dag}$ represents the stretching and reorientation by the total horizontal current field of the pre-existing ageostrophic horizontal pseudo-vorticity.

The material derivative of **TWI** is represented by the **TWI** trend forcing $\mathbf{Q}_{\mathrm{dr}}$. It is important to note that the divergence of $\mathbf{Q}_{\mathrm{dr}}$ explicitly contains the Lagrangian change of the vertical shear of the ageostrophic vertical vorticity (ζ_z^{ag}). Consequently, this means that the generalized Eq. (5) can also be interpreted in terms of the rate change of ζ_z^{ag} . As mentioned in Viùdez et al. (1996), this term has to be considered for significant ageostrophic flow with a large Rossby number, where the QG approximation is not valid, such as in fronts and eddies. In the QG and GM hypotheses, this term is set to zero, meaning that **TWI** is compensated instantaneously by the restoring effects of the ageostrophic circulation. This exact conterbalance filters inertial gravity waves and the precession of the ageostrophic pseudo-vorticity vector ($-\mathrm{TWI}(y)/f$, $\mathrm{TWI}(x)/f$, ζ^{ag}). When neglecting this term, Eq. (5) becomes purely diagnostic, as it is independent of time.

The buoyancy forcing $\mathbf{Q}_{\mathrm{th}}$ alters the horizontal density gradient by tilting the isentropic surfaces that induces a thermal-wind imbalance and thus a restoring secondary circulation that tends to cancel the ageostrophic horizontal pseudo-vorticity.

The momentum forcing $\mathbf{Q}_{\mathrm{dm}}$ modifies the horizontal current's vertical shear, which induces a thermal-wind imbalance that tends to be cancelled by the restoring ageostrophic circulation.

The **Q**-vector associated with the β-effect ($\beta = \frac{\partial f}{\partial y}$) was neglected in this study because of its very weak contribution (Fiekas et al. 1994). This forcing is expressed as $\boldsymbol{Q}_\beta = \beta v \boldsymbol{\zeta}_{ph}$ (with $\boldsymbol{\zeta}_{ph}\left(-\frac{\partial v}{\partial z}, \frac{\partial u}{\partial z}\right)$ the horizontal pseudo-vorticity) and can be added into Eq. (5) without difficulties.

To conclude, the **TWI** (or equivalently horizontal pseudo-vorticity) can be produced primarily by altering either the density field (forcing $\mathbf{Q}_{\mathrm{tw}}$ and $\mathbf{Q}_{\mathrm{th}}$) or the vertical distribution of the horizontal current (forcing $\mathbf{Q}_{\mathrm{dag}}$, $\mathbf{Q}_{\mathrm{dr}}$ and $\mathbf{Q}_{\mathrm{dm}}$).

3 Analytical approach

Although the *w*-impact of the turbulent fluxes was already discussed in Eliassen (1962) and Shapiro (1981) for 2D atmospheric frontogenesis, their role is rarely considered as a source of secondary circulation, especially in oceanic studies. It was anticipated that these terms could be important in near-surface layers and in the mixed layer (Giordani et al. 2005b).

The introduction of the turbulent buoyancy ($\mathbf{Q}_{\mathrm{th}}$) and momentum ($\mathbf{Q}_{\mathrm{dm}}$) forcing into the generalized ω-equation is the most original aspect of this paper. Their local definitions in the 3D frame (Section 2) are certainly too conceptual to allow all of the physical interpretations and the *w*-consequences [due to coupling effects between the turbulent surface fluxes and the mixed-layer depth (MLD) structures] to be derived from these forcings. To give more physical insight into these turbulent *w*-forcings, in this section, we will solve the vertical circulation in the (*x*–*z*) vertical section, forced only by prescribed analytical spatial distributions (at the surface and on the vertical) of the momentum and buoyancy turbulent fluxes and MLD, $h(x)$. The simplification of Eq. (5) to this 2D-academic case is expressed as:

$$f^2 \frac{\partial^2 w}{\partial z^2} + N^2 \frac{\partial^2 w}{\partial x^2} = \underbrace{\frac{f}{\rho}\frac{\partial}{\partial x}\left(\frac{\partial^2 \tau_{yz}}{\partial z^2}\right)}_{Dyn} \underbrace{- \frac{g}{\rho}\frac{\partial^2}{\partial x^2}\left(\frac{\partial F_\rho}{\partial z}\right)}_{Buo} \tag{12}$$

The analytical vertical distributions of the stress $\tau_{yz}(x, z)$, the buoyancy $F_\rho(x,\ z)$ and the Brunt Waïsälä frequency N^2 were prescribed in the following forms (Gaspar et al. 1990):

$$\begin{cases} \tau_{yz}(x,z) = \tau_{y0}(x)\left(1 - \frac{z^2}{h^2}\right) \\ F_\rho(x,z) = F_0(x)\left(1 + \frac{z}{h}\right) \\ \text{if } z \le -h \text{ then } N^2(z) = N_t^2 \text{ else } N^2(z) = 0 \end{cases} \tag{13}$$

Considering these expressions, the dynamical (*Dyn*) and buoyancy (*Buo*) forcings transform into:

$$Dyn = \underbrace{-\frac{2f}{\rho h^2}\frac{\partial \tau_{y0}}{\partial x}}_{D1} + \underbrace{\frac{4f\tau_{y0}}{\rho h^3}\frac{\partial h}{\partial x}}_{D2} \tag{14}$$

$$Buo = \underbrace{-\frac{g}{\rho h}\frac{\partial^2 F_0}{\partial x^2}}_{B1} \underbrace{-\frac{2g}{\rho h^3}F_0\left(\frac{\partial h}{\partial x}\right)^2 + \frac{g}{\rho h^2}F_0\frac{\partial^2 h}{\partial x^2} + \frac{2g}{\rho h^2}\frac{\partial F_0}{\partial x}\frac{\partial h}{\partial x}}_{B2}$$

$D1$ and $B1$ are the *w*-sources associated with the horizontal variability of the surface momentum $\left(\frac{\partial \tau_{y0}}{\partial x}\right)$ and buoyancy $\left(\frac{\partial^2 F_0}{\partial x^2}\right)$ fluxes. $D1$ represents the Ekman pumping and $B1$ the *w*-source due to horizontal differential heating/salting. The same expression can be found in atmospheric studies (Danard and Ellenton 1980; Giordani 1997). Terms $D2$, $B2$ are activated only when a surface energy input (τ_{y0}; F_0; $\frac{\partial F_0}{\partial x}$) and an MLD horizontal variability $\left(\frac{\partial h}{\partial x}; \frac{\partial^2 h}{\partial x^2}\right)$ occur simultaneously. Consequently, $D2$, $B2$ can be viewed as the forcing terms induced by the trapping of the surface mechanical and buoyancy energy into the mixed layer and are, thus, explicitly representative of the oceanic mixed-layer/atmosphere coupling. These forcing terms can also be interpreted in regard to vertical/horizontal modifications of the current/density fields, respectively, induced by the MLD topology. The resulting vertical velocity is set up to restore the initial balance. The trapping process is embedded and does not explicitly appear in the turbulent buoyancy and momentum **Q**-vectors. Our analytical approach allows us to split these forcing into both terms associated with the surface fluxes and MLD heterogeneities. In particular, the analytical

approach allows us to explicitly distinguish the Ekman pumping and the w-source associated with MLD variability, whereas these two processes are merged in the compact **Q**-vector form. This important point will be illustrated in a realistic case presented in Section 4.

Conditions of the experiment

The size of the vertical cross-section is defined as $x \in [0, 500\ \text{km}]$ and $z \in [-1{,}000\ \text{m}, 0]$. The analytical forms of the MLD $[h(x)]$, the surface stress $[\tau_{y0}(x)]$ and the surface buoyancy flux $[F_0(x)]$ for this experiment are given by the following expressions:

$$\begin{cases} h(x) = h_{\min} + \Delta h \sin \pi \left(\dfrac{x - x_{\min}}{x_{\max} - x_{\min}} \right) \\ \tau_{y0}(x) - \tau_{ym} \sin \pi \left(\dfrac{x}{x_{\max}} \right) \\ F_0(x) = F_m \sin \pi \left(\dfrac{x - x_{\min}}{x_{\max} - x_{\min}} \right) \end{cases} \tag{15}$$

The parameters of the experiments are given in Table 1. The surface and bottom boundary conditions are w=0, and the two lateral boundaries conditions are $\frac{\partial^2 w}{\partial x^2} = 0$ to obtain continuous and smooth behaviour of the solution at the boundaries. The vertical velocities are deduced from Eq. (12) and are completely defined by the forcing terms *Dyn* and *Buo*.

Figure 1 shows the vertical velocities that correspond to the circulation in balance with the forcing prescribed at the surface and in the mixed-layer. The vertical velocities shown in Fig. 1a are obtained when the momentum and buoyancy forcing are simultaneously activated. Two w-dipoles are clearly present. The first one is characterized by upward (positive) and downward (negative) motions in the regions [0, 150 km] and [350, 500 km], where the MLD is constant and equal to 50 m. The second one is characterized by a downward/upward motion associated with the MLD structure located in the region [200, 300 km].

The first w-dipole corresponds to the activation of forcing $D1$ only, which is associated with a cyclonic/anticyclonic zonal shear of the meridional stress: this is Ekman pumping (Fig. 1b). The second w-dipole corresponds to the activation of forcing $D2$ only, which is associated with the combined effects of the MLD variability and the surface stress intensity (Fig. 1c). This process represents the trapping of the surface mechanical energy into the mixed-layer structure. The differential redistribution of the surface momentum is induced by the MLD horizontal variability: this process is much more efficient in producing intense vertical velocities ($w_{\max} \simeq 65$ m day^{-1}) than the Ekman pumping ($w_{\max} \simeq 4$ m day^{-1}).

Compared to the dynamical forcings $D1$ and $D2$, the buoyancy forcings $B1$ and $B2$ produce vertical velocities 10–1,000 times weaker. In the present case, the variability of the surface buoyancy flux (positive density input; see Table 1) was intentionally placed in phase with the MLD anomaly (see Eq. (15)) to derive more significant vertical velocities. The vertical velocities shown in Fig. 1d correspond to the activation of forcing B_1 only, which is associated with the lumpiness of the surface buoyancy flux. This process induces downward motion of up to 29 cm day^{-1} near the bottom of the mixed-layer where the MLD is deepest and where the curvature of F_0 is the strongest. Forcing $B1$ tends to increase the density in the mixed-layer, and the vertical velocity tends to restore the spatial distribution of the density by transferring the positive density anomaly downwards. The vertical velocity corresponding to the activation of forcing $B2$ only (Fig. 1e) results from the combined effects (a) of the surface buoyancy flux F_0 and the MLD variability at the first order $\left(B2a = -\frac{2g}{\rho h^3} F_0 \left(\frac{\partial h}{\partial x} \right)^2 \right)$ and the second order $\left(B2b = \frac{g}{\rho h^2} F_0 \frac{\partial^2 h}{\partial x^2} \right)$ and (b) of the spatial variabilities of F_0 and h represented by the cross term $B2c = \frac{2g}{\rho h^2} \frac{\partial F_0}{\partial x} \frac{\partial h}{\partial x}$ (see Eq. (14)). The downward motion on the edges of the MLD structure ($\frac{\partial h}{\partial x}$ strong) reaches 30 cm day^{-1} and results from ($B2a$+$B2c$). Forcing $B2c$ induces downward motion ($w \leq 0$) and is symetrically opposite to the forcing $B2a$ ($w \geq 0$; not shown). The upward motion centred on the MLD structure reaches 16 cm day^{-1} and is induced by $B2b$, which is associated with the curvature of the MLD anomaly. Note that this contribution is opposite to the forcing $B1$. As with the dynamical forcing $D2$, $B2$ represents the trapping of the surface buoyancy energy into the mixed-layer structure or, in other words, the horizontal modification of the density field induced by the MLD variability. Finally, we mention that all of these solutions are sensitive to the thermocline stratification N^2, but this does not affect the above conclusions.

The original point of this section was to explicitly identify how the surface mechanical and buoyancy energy is trapped into the mixed-layer structure. The mechanical part of this process induces vertical velocities that are much more intense than either the buoyancy part or the Ekman pumping.

Table 1 Parameters of the academic experiment

$x_{\min}$	$x_{\max}$	$h_{\min}$	Δh	τ_{ym}	F_m	N_t^2
200 km	300 km	50 m	100 m	1 N m^{-2}	100 W m^{-2}	1e−4 s^{-2}

4 Case study

To evaluate the importance of turbulent forcing in a real situation where all forcing terms are present, we have chosen to apply the generalized ω-equation (5) to the mesoscale and sub-mesoscale structures simulated during the yearlong POMME experiment. Given the duration of the simulation, the w-inversion algorithm was conceived to

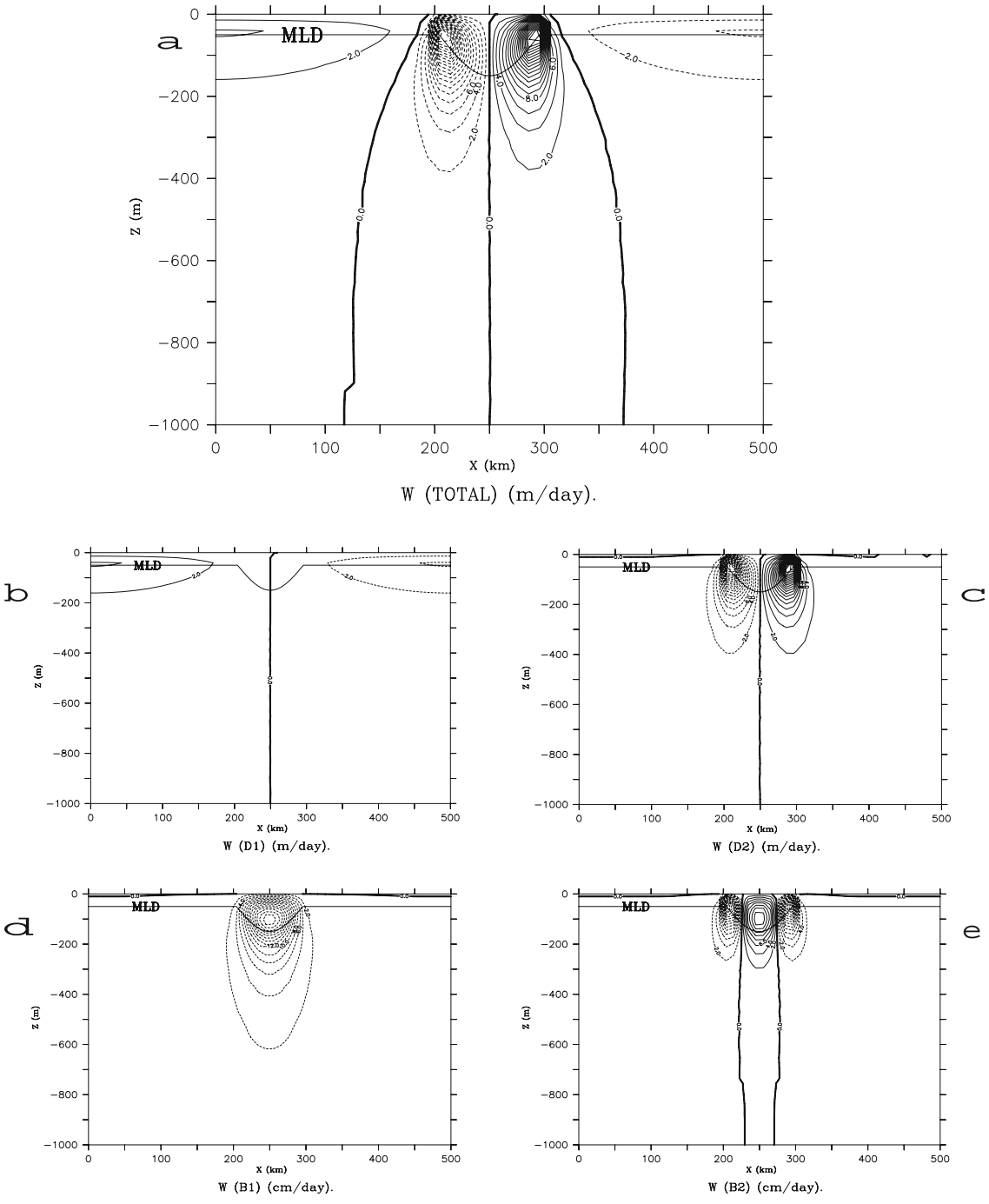

Fig. 1 **a** Total vertical velocity. **b** Ekman pumping ($D1$ forcing). **c** w-component induced by $D2$ forcing. **d** w-component induced by $B1$ forcing. **e** w-component induced by $B2$ forcing. The mixed-layer depth (MLD) is represented by the along-section continuous line. Contour intervals are 2 m day^{-1} for **a**, **b** and **c** and 2 cm day^{-1} for **d** and **e**

run on-line within a PE equation model with a minimal cost-computing. The majority of models use sequential assimilation data systems which are efficient in reducing drifts but induce shocks and spurious gravity wave radiation associated with mass circulation imbalances at each reinitialization procedure (Robinson 1996). It is well known that such imbalances/shocks strongly affect the vertical velocity and tend to generate unrealistic mesoscale and submesoscale thermodynamic and circulation structures. Consequently, Giordani et al. (2005a,b) developed a PE model which continuously assimilates analysed geostrophic currents (called guide) into the momentum equations as a substitute of the horizontal pressure gradient. This technique avoids shocks associated with sequential assimilation, authorizes geostrophic adjustment at smaller scales than the guide and allows us to perform realistic year-long simulations. By eliminating of the pressure term in the PE system, this modelling approach also filters out

the gravity waves and consequently constrains the **Q**-vector $\mathbf{Q}_{dr}$ and reduces the horizontal variability of N^2. Thus, the stratification term $\nabla_h N^2.\nabla_h w$ was approximated by $N^2 \nabla_n^2 w$ in Eq. (5), as in the QG approach. The horizontal regular grid spacing of the simulated domain is 5 km; this resolution is not sufficient to properly represent the physical gravity waves even in a full PE model. Nevertheless, at kilometric resolution, gravity waves can strongly impact on N^2 and induce non-negligible contributions to the $\nabla_h N^2.\nabla_h w$ term.

Sensitivity tests show how the *w*-structures respond to the boundary conditions. It appears that the solution of Eq. (5) is much more sensitive to the surface and bottom boundary values compared to the lateral ones. As confirmed by Pinot et al. (1996), this is because the vertical term $f^2 \frac{\partial^2 w}{\partial z^2}$ dominates the horizontal term $N^2 \nabla_h^2 w$ (Eq. (5)) near the boundaries. Nevertheless, the sensitivity of the *w*-structures to boundary conditions has been tested and found to be very weak and we decided to use w=0 as boundary conditions at the surface, bottom and four lateral boundaries.

This section presents a study of mesoscale and sub-mesoscale *w*-structures obtained during Spring 2001 of the POMME experiment, a period corresponding to intense heating and mixed-layer shoaling. This period is favourable for the formation of MLD structures, and this study is based on the validated numerical results of Giordani et al. (2005b). The daily-averaged vertical velocities on March 22 (onset of intense heating associated with moderate surface wind stress; $\tau \simeq 0.2$ N m^{-2}) at 200- and 50-m depth were superimposed onto the surface dynamic height and MLD fields, respectively (Fig. 2a,b).

At 200-m depth, intense vertical velocities are found in areas of strong gradients of surface dynamic height (Fig. 2a). These regions correspond to the frontal zone on the southern flank of a cyclonic eddy C4 (42°N), an anticyclonic eddy A1 (43°N) and the stretched frontal line delimiting high and low dynamic height regions around 18°W; 40°N. The nomenclature adopted hereafter for the eddies is the same as in Giordani et al. (2005b).

Some *w*-structures observed at 200 m are also found at 50 m, particularly those associated with the main dynamic centres. For example, the *w*-structures peripherically distributed around A1 at 200 m are also found at 50 m (Fig. 2b). The MLD displayed in Fig. 2b is in some places well correlated with the surface dynamic height (Fig. 2a), e.g. around A1, at the meridional frontal line near 18°W, 40°N and in the vicinity of C4. Nevertheless, substantial differences exist between the *w*-fields at 50 and 200 m. At 50 m (Fig. 2b), *w* displays a marked West–East filamentary and dipolar structure around 40.5°N and 18.5–20°W that does not exist at 200 m. Moreover, this *w*-structure adjusts in accordance with the MLD gradient. Such sub-mesoscale structures are of primary importance in performing realistic biological simulations (Lévy et al. 2005). In particular, concentrations of biological components are highly dependent on filamentary structures of MLD.

Figure 2a and b suggests that the *w* and dynamic height fields (a) are highly correlated and (b) show the emergence of energetic small horizontal scales near the surface which found simultaneously in the *w* and MLD fields. To better understand the physical processes that induce such *w*-organizations, we decomposed the vertical velocity into the five *w*-components associated with each of the five **Q**-vectors presented in Section 2.

Figure 3 displays the relative importance of the magnitude of each *w*-component relative to each **Q**-vector forcing at 50- and 200-m depth. The turbulent buoyancy ($w_{Q\mathrm{th}}$) and momentum ($w_{Q\mathrm{dm}}$) components are active at 50 m in the mixed-layer but $w_{Q\mathrm{th}}$ is 100–1,000 times weaker than $w_{Q\mathrm{dm}}$ and the other components. Note that the same result was found in the analytical approach (see Section 3). Clearly, the component $w_{Q\mathrm{dm}}$ provides the dominant component of the total *w*-field at 50 m displayed

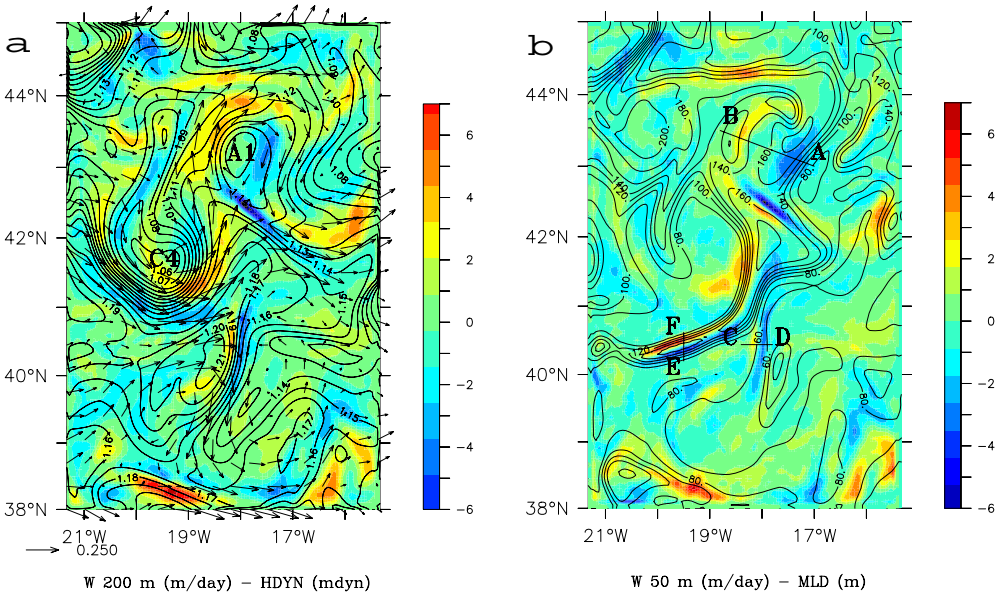

Fig. 2 **a** Daily-averaged vertical velocity at 200 m superimposed onto the surface dynamic height (mdyn) and the daily-averaged surface current (m s^{-1}) on March 22, during the POMME field experiment. The surface dynamic height is computed from the reference level 1,000 m. A1 and C4 are anticyclonic and cyclonic eddies, respectively. **b** Daily-averaged vertical velocity at 50 m superimposed onto the MLD on March 22. The situation corresponds to the onset of an intense heating associated with moderate surface stress (τ=0.2 N m^{-2}). *AB*, *CD* and *EF* represent the vertical cross-sections

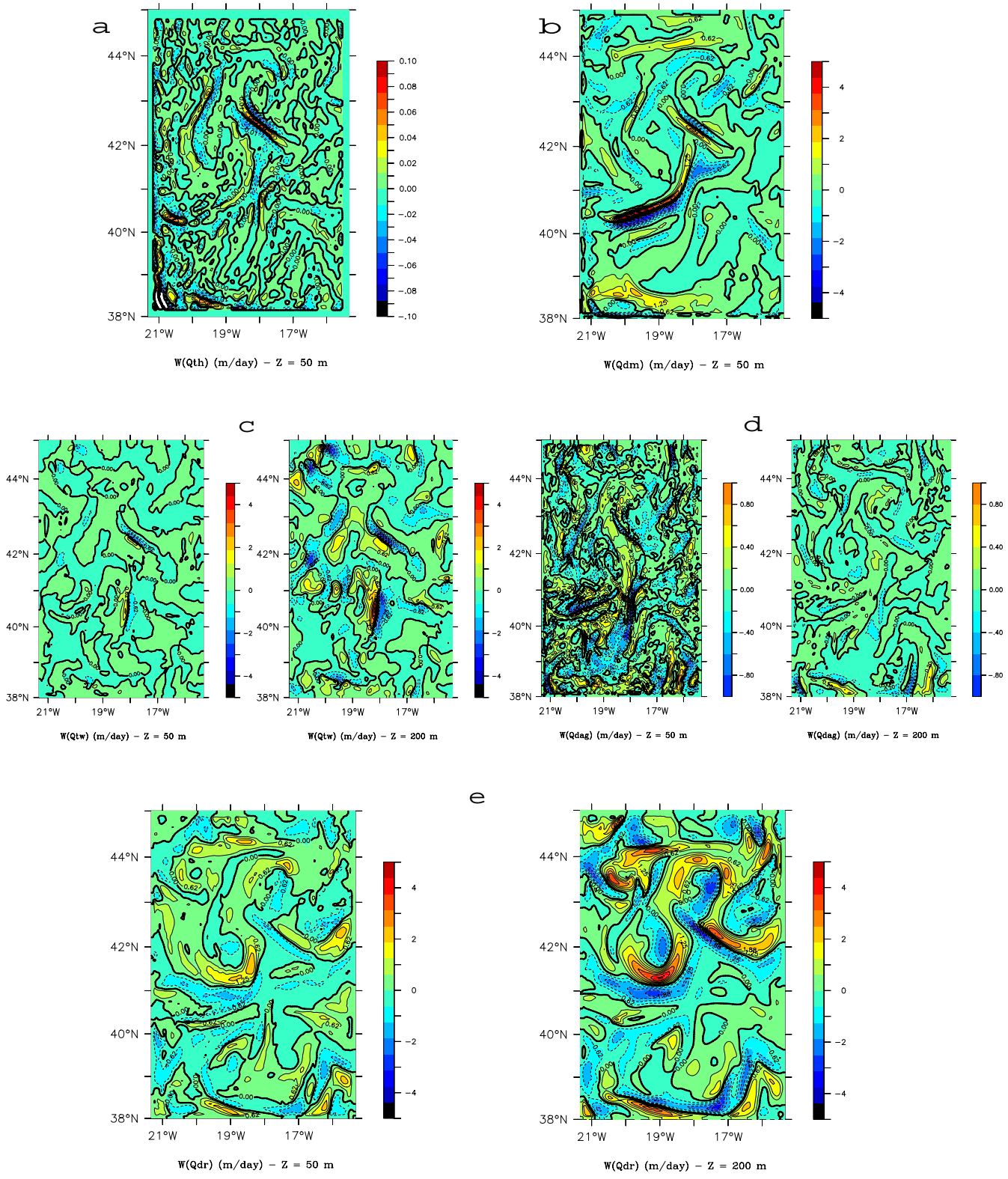

Fig. 3 Daily-averaged vertical velocity components (m day^{-1}) on March 22 at 50 m $w_{Q\mathrm{th}}$ (**a**) and $w_{\mathbf{Q}\mathrm{dm}}$ (**b**); at 50 m (*left*) and 200 m (*right*) $w_{\mathbf{Q}\mathrm{tw}}$ (**c**); $w_{\mathbf{Q}\mathrm{dag}}$ (**d**) and $w_{\mathbf{Q}\mathrm{dr}}$ (**e**)

in Fig. 2b. Specifically, the sign of the West–East filamentary structure identified at 50 m in the total w-field is established signed by $w_{Q\mathrm{dm}}$. Note that the kinematic deformation ($w_{Q\mathrm{tw}}$) and the **TWI** deformation ($w_{Q\mathrm{dag}}$) components evolve in opposite ways with depth. This means that the frontogenetic activity is stronger at 200 m than at 50 m, and the residual **TWI** is stronger at 50 m than at 200 m. The component $w_{Q\mathrm{dr}}$ is significant at both depths

because it is determined from the geostrophic adjustment which is strongly driven by the assimilated geostrophic guide. In fact, the guide imposes the evolution rate of the geostrophic dynamics and, thus, the intensity and spatial distribution of the ageostrophic circulation.

The distinct major *w*-sources depending on particular mesoscale and sub-mesoscale structures are shown in Fig. 4. Three vertical cross-sections of the total vertical velocity field and its predominant component induced by the **Q**-vector forcing are presented through (a) the anti-cyclonic eddy A1 from A (17°W; 43°N) to B (18.8°W; 43.5°N), (b) the stretched frontal line from C (18.4°W; 40.4°N) to D (17.8°W; 40.4°N) and (c) the filamentary MLD structure at 19.5°W, from E (40.2°N) to F (40.6°N) (see Fig. 2b).

The vertical cross-section AB displays a negative/positive *w*-dipole (Fig. 4a) that affects the entire thickness of the fluid (deeper than 500 m; not shown). In this cross-section, the variations of the MLD have an amplitude close to 100 m in accordance with the *w*-dipole because *w* affects the fluid up to the mixed layer. This *w*-dipole is located around the edges of A1 and is mainly explained by the

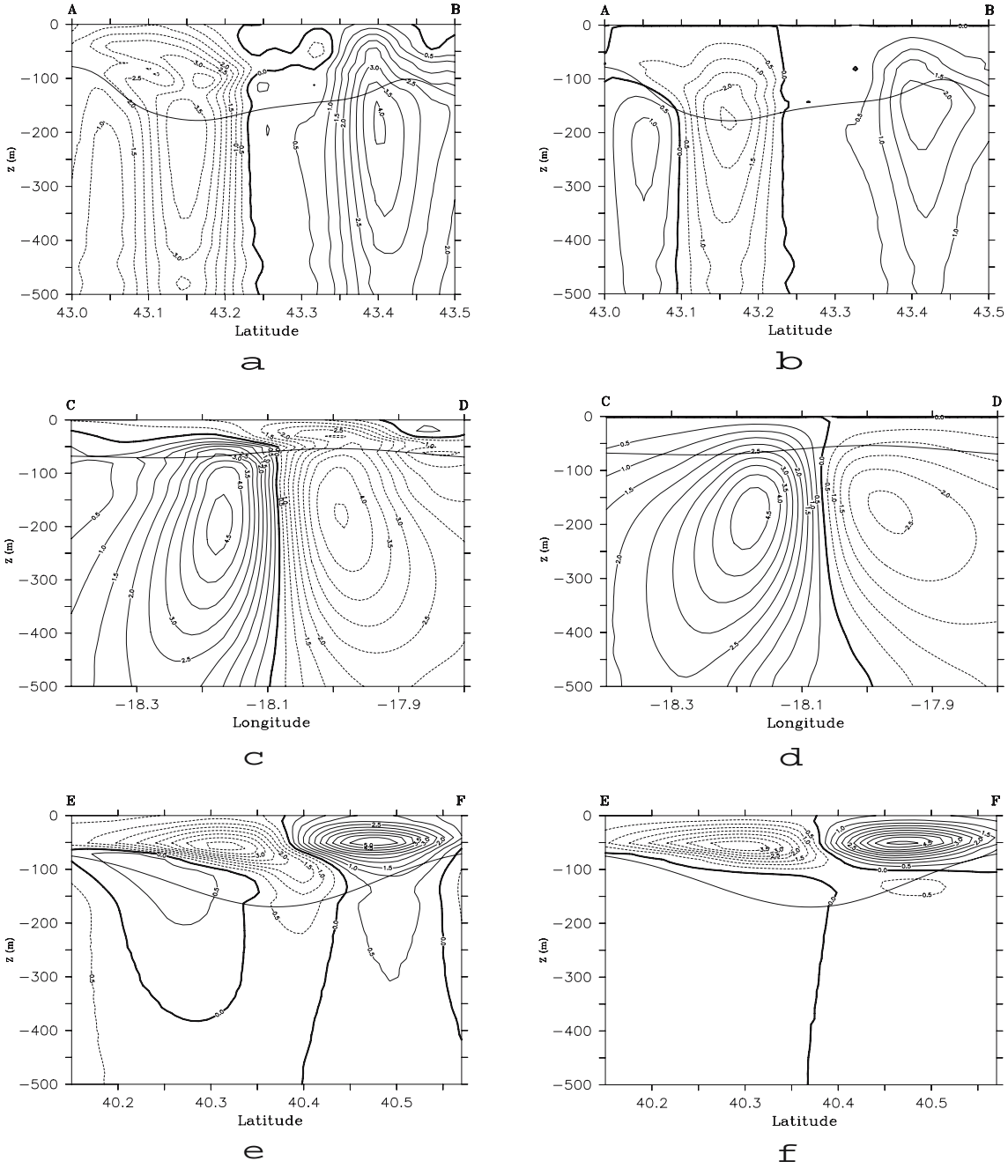

Fig. 4 Vertical cross-sections AB, CD and EF of the total vertical velocity field (m day^{-1}) (**a**, **c**, **e**) and its main *w*-component (**b**, **d**, **f**). (**b**) $w(\mathbf{Q}_{dr})$. (**c**) $w(\mathbf{Q}_{tw})$. (**d**) $w(\mathbf{Q}_{dm})$. The mixed-layer depth is represented by the *along-section continuous line*

Table 2 Correlations between the total vertical velocity with each of its five components at the level where the maximum is observed across (a) the anticyclonic eddy A1 (section AB), (b) the frontal line (section CD) and (c) the filamentary MLD structure (section EF)

	$w(\mathbf{Q}_{th})$	$w(\mathbf{Q}_{dm})$	$w(\mathbf{Q}_{tw})$	$w(\mathbf{Q}_{dag})$	$w(\mathbf{Q}_{dr})$
Cross-section AB	−0.21	0.007	0.66	0.11	**0.83**
Cross-section CD	−0.02	0.46	**0.97**	0.22	−0.19
Cross-section EF	0.07	**0.87**	0.25	0.15	0.12

Maxima of correlation are in bold numbers

forcing $\mathbf{Q}_{dr}$, as shown in Fig. 4b. This term represents the rate of change of ζ_z^{ag} , namely the vertical redistribution of the differential ageostrophic vorticity by advection. This redistribution is formally associated with the **TWI** Lagrangian change, which induces intense vertical velocities at the periphery of A1. This occurs because of significant **TWI** advection at the sub-mesoscale ($\mathbf{U}\simeq 30$ cm s^{-1}, see Fig. 2a) and local bulk displacements of A1 around its mean position (eddy A1 is moving), which are visible when the current/dynamic height fields are animated.

The vertical cross-section CD displays a positive/negative *w*-dipole, the maximum of which is around 200-m depth (Fig. 4c). This *w*-structure is mainly explained by the forcing $\mathbf{Q}_{tw}$, shown Fig. 4d. This term, also known as the frontogenesis vector, is particularly intense across the stretched frontal line shown in Fig. 2a because of the strong current and density horizontal shears. Note that $\mathbf{Q}_{tw}$ includes the ageostrophic component of the deformation field, which is as strong as the geostrophic component. Given the South–North orientation of this frontal line, the vector $\mathbf{Q}_{tw}$ is zonal and the convergence term $\left(\frac{\partial u}{\partial x}\frac{\partial \rho}{\partial x}\right)$ is its main contribution. Figure 4c shows a *w*-discontinuity across the MLD that does not exist in the *w*-field induced by the $\mathbf{Q}_{tw}$ forcing only (Fig. 4d). This discontinuity is the result of the turbulent forcings $\mathbf{Q}_{th}$ and $\mathbf{Q}_{dm}$, which disturb the frontogenesis in the mixed-layer (not shown).

In section EF, the variation of the MLD extends over 40 km (Fig. 4e). The MLD varies from 75 m (40.2°N) to 170 m (40.42°N) (amplitude 95 m over 20 km), which is clearly associated to the negative/positive *w*-dipole near the surface. This *w*-dipole is confined into the mixed layer and suggests that it could be related to surface fluxes and to the distribution of heat and momentum fluxes in the mixed layer. This assumption is confirmed by Fig. 4f, which presents the *w*-field produced by the turbulent momentum forcing $\mathbf{Q}_{dm}$. Given that the surface wind stress is constant in the domain of the MLD structure, the Ekman pumping contribution is negligible in this structure. Therefore, we conclude that the vertical velocity simulated in this real case of the POMME experiment results from the process *D*2, which describes the *w*-response induced by the coupling between the surface stress intensity and the MLD structure. This process was clarified in the analytical approach developed in Section 3. Note that the *w*-field confined in this MLD filament is completely dependent on the vertical mixing parameterization used in the model (Gaspar et al. 1990).

To quantitatively evaluate the relative importance of the **Q**-vectors for the total vertical velocity, Table 2 displays the correlations between the total vertical velocity and each of its five components at the level where the maximum is observed in the sections AB, CD and EF (see Fig. 4a,c,e). These maxima were located at 200, 200 and 50 *m* in sections AB, CD and EF, respectively. In sections AB, CD and EF, the maximum correlation reached 0.83, 0.97 and 0.87 and was associated with the forcings $\mathbf{Q}_{dr}$, $\mathbf{Q}_{tw}$ and $\mathbf{Q}_{dm}$, respectively: these correlations are confirmed by the results shown in Fig. 4. However, significant correlations (Table 2) also exist for some other *w*-sources, suggesting that these cannot be neglected. Consequently, a better description of the vertical velocity would require taking into account the following forcings: ($\mathbf{Q}_{tw}$, $\mathbf{Q}_{th}$), ($\mathbf{Q}_{dm}$, $\mathbf{Q}_{dag}$, $\mathbf{Q}_{dr}$) and ($\mathbf{Q}_{tw}$, $\mathbf{Q}_{dag}$, $\mathbf{Q}_{dr}$) in sections AB, CD and EF, respectively.

To document the vertical distribution of the main *w*-source over the period February 13–April 4 (50 days), we have calculated the correlation between the total *w* and each of its five components, averaged over that period and at each level, as shown in Fig. 5.

Two distinct dynamical regimes can be seen from the correlation profiles. The first, which affects the domain [−1,000, −120 m], namely the sub-surface ocean, is characterized by the clear dominance of the kinematic

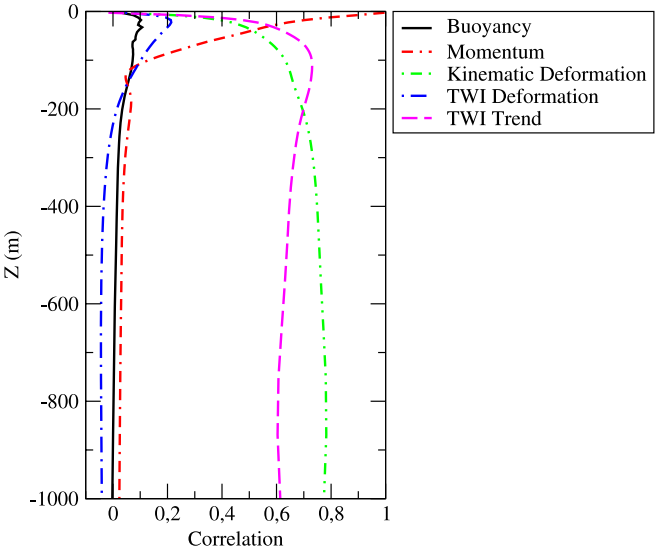

Fig. 5 Vertical distribution of the time-averaged (from February 13 to April 4; 50 days) correlation between the total vertical velocity and each of its five components

($\mathbf{Q}_{tw}$; including the geostrophic and the ageostrophic components) and **TWI** trend ($\mathbf{Q}_{dr}$) forcing. These forcings unbalance the flow by deforming the horizontal density field and by producing a differential vertical vorticity, respectively. Note that $\mathbf{Q}_{dr}$ is intense in fronts and particularly in eddies where the **TWI** advection is strong. The second regime concerns the domain [−120, 0 m], namely, the mixed-layer, and is characterized by the rapid collapse of both the $\mathbf{Q}_{tw}$ and $\mathbf{Q}_{dr}$ forcings and by the huge increase in the turbulent momentum forcing ($\mathbf{Q}_{dm}$). The contribution of the turbulent buoyancy forcing ($\mathbf{Q}_{th}$) in the mixed-layer is much weaker than the **TWI** production by deformation ($\mathbf{Q}_{dag}$). $\mathbf{Q}_{dag}$ increases in the mixed-layer because the horizontal gradients of the horizontal current are strengthened by the surface turbulent fluxes. This behaviour is also shown in Fig. 3.

We note that each w-component (not shown) has a similar relative magnitude in the vertical to that shown by the correlation analysis. This result supports the conclusions obtained from the correlation analysis.

Results show that the relative contributions of the w-sources can differ greatly when the fields are temporally/spatially averaged or considered locally. Since the vertical vorticity is much weaker than the Coriolis parameter in this study ($\zeta/f \simeq 0.08$ and $R_o \simeq 0.06$ for maximum daily-averaged values), one would conclude that the QG ω-equation is an appropriate approach for evaluating the vertical velocity. Our results show that the QG approximation is not really valid in the POMME experiment because of the important contribution of the ageostrophic forcing. This conclusion confirmed the results of Pinot et al. (1996).

5 Conclusion

This paper proposes an ocean adaptation of the generalized **Q**-vector ω-equation developed by Giordani (1997) and Giordani and Planton (2000) for the atmosphere. The ω-equation is deduced from the 3D PE system and takes into account the turbulent buoyancy and momentum fluxes. The ω-equation is applied to a regional simulation of the North-Eastern Atlantic ocean to unravel the physical processes that produce vertical velocities in mesoscale and sub-mesoscale structures.

Our approach shows that the dominant w-processes are strongly dependent on the dynamical structures (anticyclonic eddy, front, MLD structure) but also stresses the important contribution of the ageostrophic forcing even when the QG conditions are valid. This result highlights the complexity of the ageostrophic dynamics in a real case study. Note that the generalized **Q**-vector approach is useful too to quantify the impacts of a data assimilation procedure on the processes which drive the vertical dynamics in the ocean.

An original point of this paper focuses on the emergence of near-surface energetic small horizontal scales which are found simultaneously in the w and MLD fields. The study of a particular filamentary w-MLD structure of 40-km width has shown that the strong vertical velocities result from the surface mechanical energy which is trapped in the MLD structure and not from Ekman pumping. These two processes are merged in the forcing and do not explicitly appear in the turbulent momentum **Q**-vector but were revealed using an analytical approach. The same decomposition was obtained with the turbulent buoyancy **Q**-vector, but this forcing was found to be much weaker than the turbulent momentum forcing. This identification of how the surface buoyancy and mechanical energy are trapped into the mixed-layer structures is an original finding. This process is able to induce vertical velocities that are much more intense than those involved by Ekman pumping and is also more representative of the atmosphere/oceanic mixed-layer coupling. The process could also improve our understanding of the complex dynamics of the near-surface layers (e.g. vortex filaments, Lapeyre and Klein, 2006, in press) and certainly has important applications for biological tracers trapped into filamentary MLD structures. In particular, this paper proposes a separation of the mesoscale stirring and turbulent (buoyancy and momentum) forcing in the generalized ω-equation, which could certainly improve our understanding of the spatial distribution of the vertical pump in the oceanic upper layers.

The ω-equation inversion algorithm used in this study was conceived and adapted to run on-line in an ocean model and is thus a robust and low-cost numerical diagnostic tool for computing vertical velocities. This algorithm can also be used on gridded observed (ADCP and CTD), analysed, climatological and 3D model data. It could be fruitful to provide this algorithm to the oceanographic community to study the vertical velocity from the sub-mesoscale up to synoptic and climate scales.

Acknowledgements We are grateful to Rosemary Morrow, Anna Pirani and our two anonymous reviewers for their help in revising this manuscript and to Youcef Amar for his valuable technical assistance.

This work was supported by the French programs PATOM and PROOF (CNRS/INSU).

References

Danard MB, Ellenton GE (1980) Physical influences on east coast cyclogenesis. Atmos Ocean 18:65–82

Davies-Jones R (1991) The frontogenetical forcing of secondary circulations. Part I: the duality and generalization of the Q-vector. J Atmos Sci 48:497–509

Eliassen A (1962) On the vertical circulation in frontal zones. Geofys Publ 24:147–160

Fiekas V, Leach H, Mirbach K-J, Woods JD (1994) Mesoscale instability and upwellwing. Part I: observations at the North Atlantic intergyre front. J Phys Oceanogr 24:1750–1758

Fischer J, Leach H, Woods JD (1989) A synoptic map of isopycnic potential vorticity in the seasonal thermocline. J Phys Oceanogr 19:519–531

Gaspar P, Grégoris Y, Lefèvre JM (1990) A simple Eddy kinetic energy model for simulations of the oceanic vertical mixing: tests at station Papa and long-term upper ocean study site. J Geophys Res 95:16179–16193

Giordani H (1997) Modélisation de la Couche Limite Atmosphérique Marine en présence d'un front thermique océanique : application à la campagne SEMAPHORE. Ph.D thesis, Université Paul Sabatier, Toulouse

Giordani H, Planton S (2000) Modeling and analysis of ageostrophic circulation over the Azores Oceanic Front during the SEMAPHORE experiment. Mon Weather Rev 128:2270–2287

Giordani H, Caniaux G, Prieur L (2005a) A simplified oceanic model assimilating geostrophic currents: application to the POMME experiment. J Phys Oceanogr 35:628–644

Giordani H, Caniaux G, Prieur L, Paci A, Giraud S (2005b) A one year mesoscale simulation of the Northeast Atlantic: mixed layer heat and mass budgets during the POMME experiment. J Geophys Res 110:C07S08. DOI 10.1029/2004JC002765

Hoskins BJ, Draghici I, Davies HC (1978) A new look at the w-equation. Q J R Meteorol Soc 104:31–38

Keyser D, Pecnick MJ (1987) The effect of along temperature variation in a two-dimensional primitive equation model of surface frontogenesis. J Atmos Sci 44:577–604

Lapeyre G, Klein P (2006) Dynamics of the upper layers in terms of surface quasi-geostrophy theory. J Phys Oceanogr (in press)

Leach H (1987) The diagnosis of synoptic-scale vertical motion in the seasonal thermocline. Deep Sea Res 34:2005–2017

Lévy M, Gavart M, Mémery L, Caniaux G, Paci A (2005) A 4D-mesoscale map of the spring bloom in the northeast Atlantic (POMME experiment): results of a prognostic model. J Geophys Res 110:C07S21. DOI 10.1029/2004JC002588

Mémery L, Reverdin G, Paillet J, Oschlies A (2005) Introduction to the POMME special section: thermocline ventilation and biogeochemical tracer distribution in the North–East Atlantic Ocean and impact of mesoscale dynamics. J Geophys Res 110: C07S01. DOI 10.1029/2005JC002976

Pinot JM, Tintoré J, Wang D-P (1996) A study of the omega equation for diagnosing vertical motions at ocean fronts. J Mar Res 19:239–259

Pollard RT, Regier LA (1992) Vorticity and vertical circulation at an ocean front. J Phys Oceanogr 22:609–625

Robinson AR (1996) Physical processes, field estimation and interdisciplinary ocean modelling. Earth Sci Rev 40:3–54

Shapiro MA (1981) Frontogenesis and geostrophically forced secondary circulations in the vicinity of jet stream-frontal zone systems. J Atmos Sci 38:954–973

Strass Volker H (1994) Mesoscale instability and upwellwing. Part II: testing the diagnostics of vertical motion with a three-dimensional ocean front model. J Phys Oceanogr 24:1759–1767

Tintoré J, Gomis D, Alonso S (1991) Mesoscale dynamics and vertical motion in the Alborán Sea. J Phys Oceanogr 21:811–823

Viùdez A, Tintoré J, Haney RL (1996) About the nature of the generalized omega equation. J Atmos Sci 53:787–795